2014

Development and application of a novel precession electron diffraction technique to quantify deformation structures in a highly deformed material – ultrafine grained titanium

Iman Ghamarian, *University of North Texas*
Yue Liu, *University of North Texas*
Peyman Samimi, *University of North Texas*
Peter C. Collins, *University of North Texas*

Available online at www.sciencedirect.com

ScienceDirect

Acta Materialia 79 (2014) 203–215

Acta MATERIALIA

www.elsevier.com/locate/actamat

Development and application of a novel precession electron diffraction technique to quantify and map deformation structures in highly deformed materials—as applied to ultrafine-grained titanium

Iman Ghamarian [a], Yue Liu [a,b,c], Peyman Samimi [a,b,c], Peter C. Collins [a,b,c,*]

[a] Department of Materials Science and Engineering and the Center for Advanced Research and Testing, University of North Texas, Denton, TX 76203, USA
[b] Center for Advanced Non-Ferrous Structural Alloys (CANFSA), An NSF I/UCRC between the University of North Texas, Denton, TX 76203, USA
[c] The Colorado School of Mines, Golden, CO 80401, USA

Received 25 February 2014; received in revised form 25 June 2014; accepted 26 June 2014

Abstract

The increased spatial resolution of a new characterization technique, precession electron diffraction (PED), makes possible the very accurate and automated quantitative characterization of technically interesting materials that historically have been difficult to analyze due to their dimensions and/or degree of deformation, including specifically ultrafine-grained metallic structures with high dislocation densities. PED, when coupled with the novel post-processing techniques that have been rigorously developed and presented for the first time in this paper, such as applying a Kuwahara filter to improve the angular resolution of the technique, makes it possible to determine grain size, texture, the density and spatial distribution of geometrically necessary dislocations, crystal orientation gradients, and the character of grain boundaries at the relevant length scale (the nanoscale) for such ultrafine-grained materials. The methods detailed in this paper place the determination of key microstructural features on a quantitative, rather than qualitative footing. These techniques have been applied to a hexagonal close-packed α-titanium. The results include the correlation between defect structure and microstructure with a nanometer resolution, the identification of regions containing few geometrically necessary dislocations, the quantification of dislocation densities in cell walls, and the quantification of deformation type in a statistically meaningful fashion.

Keywords: Precession electron diffraction; Ultrafine-grained materials; Dislocation density; Geometrically necessary dislocations; Titanium

1. Introduction

It is well known that the interaction of the defect structure (e.g. dislocations) of a material with the corresponding microstructures significantly affects the properties of the material. Indeed, it would be highly desirable to correlate in a statistically meaningful manner the defect structure and the microstructure. Such information would provide a means for predicting many properties, e.g. the full elastic/plastic tensile response as well as fatigue. Hence, the rigorous characterization of a material requires an analysis of not only the microstructure, but also the attending defect structures. This is not necessarily an easy task to accomplish in a truly quantitative manner for most materials. There are methods, including both diffraction-contrast transmission electron microscopy (TEM) techniques [1,2] and emerging scanning electron microscopy (SEM)-based techniques [3,4], to image dislocations present in a material. In general, such studies are limited to materials that have

* Corresponding author at: Department of Materials Science and Engineering and the Center for Advanced Research and Testing, University of North Texas, Denton, TX 76203, USA. Tel.: +1 940 565 4630; fax: +1 940 565 4824.
E-mail address: Peter.Collins@unt.edu (P.C. Collins).

http://dx.doi.org/10.1016/j.actamat.2014.06.063
1359-6454/

been subjected to limited low degrees of deformation with low to intermediate levels of dislocations.

However, when either the bulk or localized density of the dislocations is quite high, such as found in highly deformed materials, the characterization of such materials has traditionally been rather difficult. So-called ultrafine grained (UFG) materials are an example of such highly deformed materials and have received considerable attention [5–14]. UFG materials are characterized by a significant increase in yield and tensile strengths, owing to an increase in dislocation density that promotes Taylor hardening [15,16], without necessarily a concurrent reduction in ductility. While small grains (<200 nm) and an increase in dislocation density ($>10^{15}$ m^{-2}) result in attractive material static properties, they make the accurate characterization of such materials very difficult. For example, although complex fitting of the X-ray diffraction spectrum can be used to model bulk average dislocation densities and bulk average non-deformed crystallite sizes [17,18], these efforts have a relatively large degree of uncertainty, are limited to average values, and cannot be used to unfold the interrelationships that may exist between defect structures (e.g. dislocation distribution with respect to grain boundaries and/or triple junctions [19]). Conversely, electron backscattered diffraction (EBSD) techniques can be used to quantify texture, grain size and spatial distributions of strain gradients, but are limited ultimately in their spatial resolution (e.g. 20–30 nm in minimally deformed materials [20] and 100 nm in more highly deformed materials [21,22]). The angular resolution can approach 0.5° [23]. EBSD has been used to study the microstructural evolution [24], strain gradients [25] and dislocation density [4,19,26–28] of various materials. Regrettably, as the overall quality of electron backscattered patterns degrade when the crystal lattice is highly deformed [29], such orientation microscopy techniques cannot be adopted easily for severely deformed metallic materials.

A new characterization method, precession electron diffraction (PED), has been developed and offers exceptional spatial resolution (~2 nm) owing to the ~0.5–1.0 nm probe size and reasonable angular resolution, reported to be better than ~0.8° [30]. In addition to being related to the dispersion of diffracted beams (a function of strain, step size and sample thickness), the angular resolution is related to the crystal symmetry, the proximity to a zone axis, and the ratio of signal to noise in the diffraction pattern. This latter variable will be a function of microscope and experimental conditions (e.g. temperature of the specimen, and specimen thickness). For this paper, the authors assume a worst-case scenario of 0.8°. The PED technique automatically collects spot diffraction patterns, which are less sensitive to lattice distortions in highly deformed materials, in a pre-defined raster pattern and subsequently determines local crystal orientation by comparing the experimentally acquired diffraction patterns vs. pre-calculated diffraction patterns [30,31]. In this way, it is rather analogous to the EBSD method. Importantly, the PED technique effectively eliminates phenomena that arise due to dynamic diffraction, including Kikuchi lines, double diffraction and residual background intensity. Consequently, the quasi-kinematic diffraction patterns can be matched against calculated kinematic patterns, and the local beam orientation assigned.

This paper presents the analytical techniques required to exploit the advantages of PED in order to map the spatial variation of geometrically necessary dislocation (GND) densities and consequently extract quantitative information (e.g. average GNDs, cell sizes, grain boundary character and its distribution, etc.), and considers the practical limitations of TEM (e.g. specimen thickness) to inform the associated limitations of the techniques. While the motivation for the development of the methods presented in this paper is the investigation of UFG commercially pure titanium, this method is easily extendable to other materials. With respect to UFG materials, most studies have been limited to data snapshots of microstructural evolution associated with the material processing using laboratory-scale systems [7,9,32]. This approach will allow a richer interrogation of microstructure and defect structures, including: dislocation distributions and densities, presence of nascent recrystallized grains, grain boundary characterization, grain size, cell size, intragranular misorientation (orientation gradients within a single grain) and texture.

2. Experimental approaches

The TEM specimens were prepared from bulk UFG commercially pure Ti using conventional dimpling and argon ion milling using a Fischione 1010 Ion Mill. An FEI Tecnai G2 F20 S-Twin FEG scanning/transmission electron microscope operating at 200 keV and a spot size of ~1 nm (i.e. spot size 9 on the FEI Tecnai [22]) was used for all analytical approaches and to obtain the results presented below.

The PED experiments were conducted using a state-of-the-art NanoMEGAS (Brussels, Belgium) hardware and software package [31]. This hardware associated with PED optically couples with the TEM to drive beam scan and tilt coils, enabling an external computer to scan in real space a very well-aligned probe across a predefined area of the specimen, and collect diffraction patterns using an external high frame rate camera (Stingray F-046, Allied Vision Technologies).

2.1. Precession electron diffraction—theory

Given the relative infancy of these techniques, the theory of precession electron diffraction is presented as follows and is illustrated in the five schematics given in Fig. 1a–e [33]. As is the custom for such TEM schematics where real angles of beam tilt and deviation from ideal Bragg diffraction are quite small (~0.5–1°), the angles shown in Fig. 1a are highly exaggerated for visualization purposes.

The ray diagram given in Fig. 1a illustrates that the beam is taken off-axis (~0.5–3.0°) by the upper deflection ("beam tilt") coils and precessed about the optic axis.

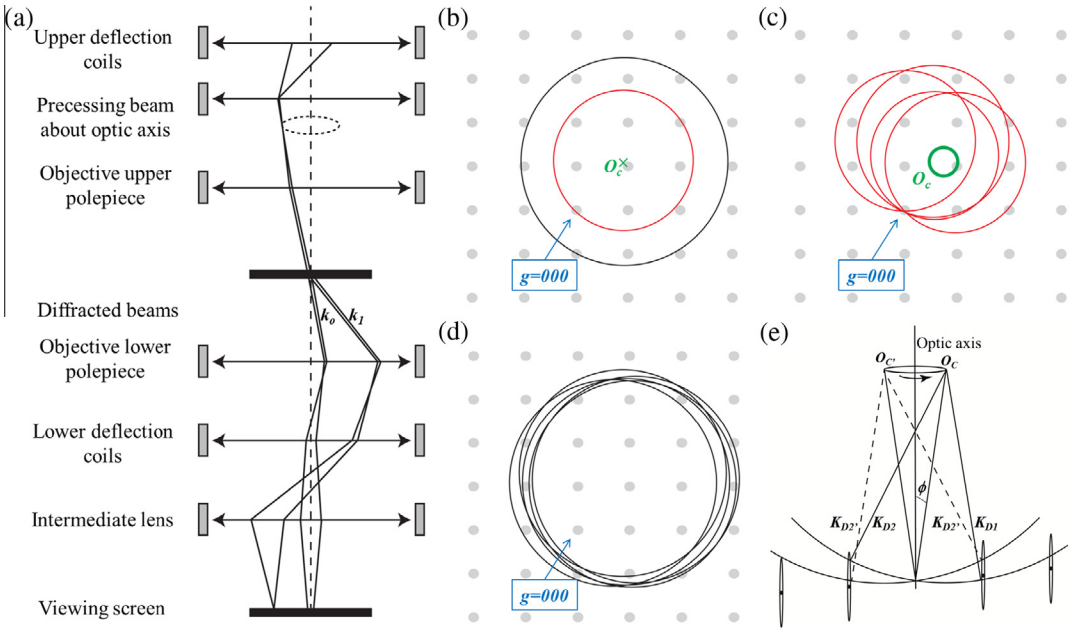

Fig. 1. Schematics of precession electron diffraction with, as is typical for visualization purposes, highly exaggerated angles: (a) ray diagram; (b) the original intersection (red circle) of the Ewald sphere with the reciprocal lattice and slice through reciprocal lattice rods (gray circle) without precession, where O_C is the projection of the center of the Ewald sphere; (c) the intersections of the Ewald sphere with the lattice as it is "rocked" due to the beam precessing, where O_C is the projection of the precessing center of the Ewald sphere; (d) the slice through reciprocal lattice as the beam precesses; and (e) "side view" of the rocking of the Ewald sphere, where it is clear that O_C is the precessing center of the Ewald sphere. (For interpretation of the references to color in this figure legend, the reader is referred to the web version of this article.).

The upper pole piece brings the precessed beam to a focused probe at the specimen. In diffraction mode, the specimen diffracts the incident beam, resulting in precessed transmitted and diffracted beams. For simplicity, only one diffracted beam is illustrated. Following diffraction, the lower deflection (beam tilt) coils are used to descan the post-specimen precession, resulting in a diffraction pattern that is focused. Fig. 1b illustrates the intersection of the reciprocal lattice with the Ewald sphere. The red circle is where the Ewald sphere cuts through the lattice plane, whereas the black circle circumscribes the points that might be visible owing to the presence of reciprocal lattice rods (rel-rods). The position O_C is the projection of the center of the Ewald sphere. Note $\mathbf{g} = \mathbf{000}$, which is the transmitted beam. As the beam is precessed (O_C is represented as a precessed circle and no longer as a point) and the Ewald sphere is rocked (see Fig. 1c–e), the intersection of the Ewald sphere with the lattice (red circles, Fig. 1c), specifically both its size and orientation, will change, while remaining "fixed" to $\mathbf{g} = \mathbf{000}$. However, the region of diffracted intensities owing to the interaction of the Ewald sphere with the rel-rods essentially has a series of overlapping circles (see Fig. 1d). The side view (along the optic axis) of this rocking is shown in Fig. 1e.

These interactions effectively eliminate features commonly associated with dynamic diffraction, including double diffraction and systematic intensity variations within a particular **g**. Further, the background intensity is reduced greatly. Thus, by using PED, the beam intensities may be calculated and compared with kinematic solutions to determine the local crystal orientation. Consequently, PED is said to be quasi-kinematic.

2.2. Operation of the NanoMEGAS system

After aligning the microscope and PED system [31], a converged beam was precessed about the optic axis at an angle of 1.3°. An exposure time of 60 ms was used to collect each diffraction pattern. While not an explicit variable, the exposure time and precession frequency (100 Hz) can be used to determine precession averaging, analogous to frame averaging for electron backscattered diffraction studies. For this work, the precession averaging was six precessed cycles/exposure. The diffraction patterns were collected as 144 × 144 pixels at a camera length of 71 mm. A step size of 10 nm was used for this study, though, in principle, the step size can range from ~0.5 nm (the size of the smallest probe) to 0.1–1 μm. Arguably, both diffraction and the precessing of the beam [30] will increase the effective probe diameter within the specimen (e.g. estimated to be ~3–5 nm for a 0.5 nm probe in a thick specimen). Thus, if a step size is selected that is less than this minimum effective probe size, information from the same small volume will be sampled for multiple steps, in essence oversampling the sample.

Once collected, the datasets ("Blockfiles", site-specific diffraction patterns, e.g. Fig. 2a–c) are matched against databases of >1000 simulated diffraction patterns (i.e. "banks"), resulting in the automated identification of the local crystal phase/orientation. Once the local crystal

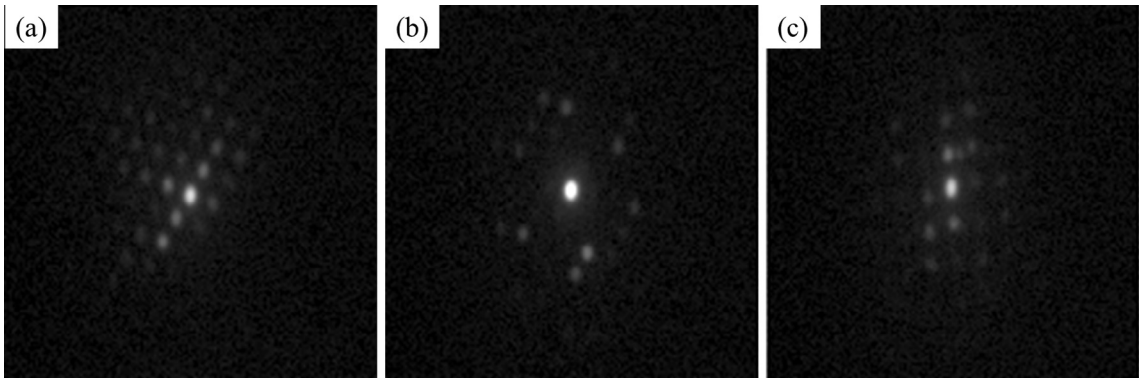

Fig. 2. (a–c) Three prototypical diffraction patterns collected from different points on an UFG Ti specimen collected using NanoMEGAS software.

phase/orientation has been determined relative to the beam, it is possible to directly export and post-process the .ang files as one would with more traditional EBSD datasets.

2.3. Post-processing of data

Various post-processing techniques have been used, including NanoMEGAS software, TSL software and MATLAB codes developed for this work, and these are described below.[1] All post-processing was conducted on an eight-core XEON, 2.4 GHz, Dell Precision T3600.

3. Analytical approaches

It is necessary to set a threshold for both grain and cell boundaries, in order to avoid having, for example, neighboring pixels in an adjacent grain or misindexed points inside a grain contribute to the averaging. Regarding the definition of grain boundaries, often, and somewhat arbitrarily, a relative misorientation threshold (i.e. ΔX°) is used to set the definition of a grain boundary (often $\sim 5^\circ$). The results presented below allow ΔX° to vary in the range of 2–5°.

3.1. Use of quaternion averaging to improve angular resolution

Recently, methods to improve the angular resolution of conventional SEM-based high-resolution EBSD orientation studies have been reported, with notable improvements to the angular resolution while simultaneously preserving boundaries. Effectively, these papers have shown that it is possible to reduce the noise that is present in the orientation data and consequently smooth the IPF map [34,35]. These have made use of quaternion averaging, which averages the misorientation between two data points. Subsequently, the Kuwahara filter [34] allows for a pixel to adopt a region-averaged value. Interestingly, in previous SEM-based EBSD studies, it was suggested that this smoothing method is inappropriate for post-processing of EBSD datasets of highly deformed materials due to the presence of large misorientation gradients [34]. However, for datasets obtained using PED and depending upon both the probe size and specimen thickness, the step size can be of the order of 1–5 nm, effectively increasing the number of discrete observations along a misorientation gradient, reducing the pixel-normalized change in angle, and allowing these smoothing algorithms to be exploited.

3.2. Calculation of dislocation density (geometrically necessary dislocations)

Briefly, GNDs are those that are associated with a measurable lattice rotation, although at a certain scale and with a certain "window size", every dislocation can be considered as a GND [16,36]. GNDs generally align themselves to accommodate curvature, while statistically stored dislocations (SSDs) move and glide during deformation to relax the stress [37]. It is useful to understand the nature of dislocations as both discrete entities and as aggregate populations within a material to interpret Taylor hardening and plastic deformation under different static, cyclic and thermal loads [38]. For example, work hardening in homogeneously deformed single crystals is attributed to SSDs, whereas GNDs play a key role in work hardening of heterogeneously deformed polycrystalline materials after a specific amount of deformation at which GND density exceeds SSD density [39–41].

Recently, efforts have been made to estimate the minimum density of GNDs from EBSD-based orientation maps. A rough approximation of GND density from simple tilt and twist boundaries can be calculated using the following equation[2] [9,42]:

$$\rho \approx \frac{\gamma.\theta}{\boldsymbol{b}.l}, \tag{1}$$

where $\gamma_{tilt} = 1$, $\gamma_{twist} = 2$, θ is the local misorientation value, $\boldsymbol{b}$ is the Burgers vector ($|\boldsymbol{b}| = 0.295$ nm for $\langle \boldsymbol{a} \rangle$-type

[1] The reader should be aware that there is a difference in the frame of reference for both ASTAR and TSL (TSL OIM; EDAX, Mahwah, NJ). For completeness, the reader is referred to Ref. [22].

[2] Following convention, scalars are designated as *italics*, vectors are designated as ***bold italics***, and tensors are *italics* with the common subscripts. Diffraction pattern reflections (i.e. g-vectors) are presented in **bold**.

dislocations in an α-phase Ti) and l is the scanning step size. The identical equation can be deduced for PED, which can be used to calculate the number of dislocations in a given cross-section of the foil.

While this simplified form is attractive, it has inherent limitations owing to the exclusion of the Nye tensor. A more accurate method to estimate the lower bound of the dislocation density has been proposed by Pantleon [40] in which infinitesimal lattice rotation components are derived from finite lattice rotations, i.e. the misorientation between a Bunge Euler set and its neighbors [43]. In this method, the lower bound of the GND density is calculated from the lattice curvature components according to Eqs. (2), 6–9. Following convention, in this work, the elastic strain tensor is assumed to be zero.

In general, it is expected that as the average spacing between the dislocations decrease (i.e. the dislocation density increases), the elastic strain will begin to become important. If the dislocation density is sufficiently large, there are various ways to treat the elastic strain. A dislocation density of $10^{16}\,m^{-2}$ corresponds to an average spacing of 10 nm between any two dislocations. Similarly, a dislocation density of $4\times10^{16}\,m^{-2}$ corresponds to an average spacing of 5 nm between any two dislocations. For screw dislocations, these correspond to elastic strains of 0.23% and 0.46%, respectively. These two values have been chosen as an "average" and a "high" dislocation density as determined in this study. Such a small degree of elastic strain is confirmed through XRD where the lattice parameters match those of undeformed titanium to a level of better than 0.2%.

Given that the elastic strain tensor is assumed to be zero, and this has been shown to be a valid assumption at the level of dislocation density observed in these and similar materials [44], the elastic distortion tensor is equivalent to the lattice rotation tensor. Consequently, the local lattice rotation can be related to the disorientation (smallest misorientation) between two adjacent pixels according to the following equation:

$$\Delta \boldsymbol{w} = \frac{2\cos^{-1}\Delta q_0}{\sqrt{1-\Delta q_0^2}}\Delta \boldsymbol{q}, \tag{2}$$

where $\Delta \boldsymbol{q}$ is the disorientation between two adjacent points and their corresponding orientation sets. As crystal structures have symmetry, the same orientation can be represented by different orientation sets. To determine the smallest misorientation between any two sets, crystal symmetry elements must be applied to both sets to find the equivalent orientation sets which make the smallest misorientation:

$$\Delta g = C_{i1} g_1 (C_{i2} g_2)^T \tag{3}$$

$$\Delta g' = C_{i2} g_2 (C_{i1} g_1)^T \tag{4}$$

$$\theta = \min\left\{\cos^{-1}\left(\frac{\Delta g_{11}+\Delta g_{22}+\Delta g_{33}-1}{2}\right), \cos^{-1}\left(\frac{\Delta g'_{11}+\Delta g'_{22}+\Delta g'_{33}-1}{2}\right)\right\} \tag{5}$$

where C_{iX}, g_X and θ represent, respectively: crystal symmetry matrices ($i=1$ to 12 for the hexagonal close-packed (hcp) α-Ti crystal structure [45] and X is an orientation set), the orientation matrix for orientation set X, and the smallest disorientation[3] angle of all the misorientation matrices (Δg and $\Delta g'$).

The distortion value can be used to calculate the lattice curvature components according to the following equation:

$$\kappa_{kl} = \frac{\partial w_k}{\partial x_l} \tag{6}$$

where k and l are from 1 to 3, referring to the principal directions. Following the calculation of the lattice curvature, the local lattice rotation can be calculated from an adjacent pair of nearest neighbors of a pixel. Given that all the acquired orientation values are for a 2-D projection of a 3-D volume, it is impossible to calculate every component of the Nye tensor. Six components of the lattice curvature can be determined from local orientation measurements on planar surfaces. Using these six lattice curvature components, it is possible to determine five components of the dislocation density and one difference between two other components [40]. The five components of the dislocation density tensor and the four missing components are given in Eqs. (7) and (8), respectively [40]:

$$\begin{aligned}
\alpha_{12} &= \kappa_{21}\\
\alpha_{13} &= \kappa_{31}\\
\alpha_{21} &= \kappa_{12}\\
\alpha_{23} &= \kappa_{32}\\
\alpha_{33} &= -\kappa_{11}-\kappa_{22}
\end{aligned} \tag{7}$$

$$\begin{aligned}
\alpha_{11} &= -\kappa_{22}-\kappa_{33}\\
\alpha_{22} &= -\kappa_{11}-\kappa_{33}\\
\alpha_{31} &= \kappa_{13}\\
\alpha_{32} &= \kappa_{23}
\end{aligned} \tag{8}$$

Once these components are calculated, the lower bound of the GND density is the summation of the calculated Nye's tensor components:

$$\rho_{GND} = \frac{1}{b}\left(|\alpha_{12}|+|\alpha_{13}|+|\alpha_{21}|+|\alpha_{23}|+|\alpha_{33}|\right) \tag{9}$$

In reality, as Eq. (9) contains a limited number of lattice curvatures, it is less useful for hcp structures where there exist multiple slip systems (e.g. both $\langle \boldsymbol{a}\rangle$-type and $\langle \boldsymbol{c}+\boldsymbol{a}\rangle$-type dislocations). One potential approach that can be followed to overcome this limitation is the minimization of the total dislocation line energy [19,43].

[3] Keeping to convention, as this approach determines the smallest misorientation, the term disorientation will be adopted where appropriate from this point on in the paper, and will convey this meaning.

4. Results and discussion

4.1. Raw data obtained using precession electron diffraction

Fig. 3a–g provides examples of the types of data that are readily extractable from a representative PED dataset of UFG Ti. Fig. 3a shows an index map that graphically illustrates the closeness of fit between the simulated and acquired diffraction patterns, somewhat analogous to EBSD image quality maps. However, whereas image quality maps may be subsequently processed to determine local strains, the contrast variation (closeness of fit) of PED index maps are more complex, and may exhibit contrast variations arising from (for example): specimen thickness, overlapping diffraction patterns from multiple crystals or phases, experimental conditions (exposure and camera bit settings) and crystal symmetry. Fig. 3a,b provide an example illustrating a case where the brightness does not correspond to the degree of residual strain. The nascent (recrystallized) grain in the sub-region labeled "1" in Fig. 3a), as determined from a kernel average misorientation (KAM) [46] plot (see Fig. 3b), is identified by an arrow in Fig. 3a and appears darker, even though there is less strain.

The current analysis techniques for grain boundaries and texture are equivalent for PED and EBSD. Regarding the analysis of grain boundaries, the conventional method seeks to categorize grain boundaries as either low or high misorientation angle. However, there exist two new methods. The first, proposed by Patala and Schuh [47], incorporates quaternions and can provide both the misorientation angle and the misorientation axis (i.e. the common axis to both grains). The second, developed by Rohrer and co-workers [48,49], uses stereological methods to capture the distribution of grain boundary traces, and, based upon the non-universal assumption that there is a dominant minimum energy boundary configuration for every unique disorientation, enables the grain boundary plane to be deduced. For this analysis, Patala and Schuh's approach has been applied to the sub-region labeled "2" in Fig. 3a, and the results are presented as an overlay with the index map (Fig. 3c), with the corresponding legend shown in Fig. 3d. Since the sectioning planes containing larger disorientations are not fully within the fundamental zone, the triangles are truncated [47]. It should be noted that the darker and lighter contrasts/colors belong to high-angle and low-angle misorientations, respectively. The grain boundary misorientation angle can be found easily by matching the color of the grain boundary with the color legend. The grain boundary axis also can be determined by the location of the matched color in the triangle. Interestingly, as TEM is inherently a 2-D representation of a finite 3-D volume, there is an opportunity to characterize unambiguously the grain boundary plane, misorientation axis and misorientation angle without inducing the stereological metrics required by Rohrer. This would be by conducting manual tilt or automated tomographic tilt experiments and fusing the microstructure (grain boundary) with the orientation data.

For interpretation of the grains themselves the disorientation plot (see Fig. 3e) reveals more information than is afforded by the frequently used inverse pole figure (IPF) maps in which grains are represented based on crystallographic vectors perpendicular to the viewing plane [47]. Fig. 3e can also be interpreted based on the color legend shown in Fig. 3d. One observation which is immediately clear from Fig. 3e is that there exist local disorientations which, though significant, are less than a threshold required for a grain boundary. However, when considering the point-to-origin disorientation, the gradients can be quite significant (e.g. >20–30°). Other common orientation microscopy inspired post-processing techniques, such as texture analyses (Fig. 3f) or grain size measurements (Fig. 3g), are possible for PED datasets.

4.2. Quaternion averaging, the Kuwahara filter and angular resolution

The results presented below have been processed using quaternion averaging by applying the Kuwahara filter to improve the angular resolution to a level of ~0.4° (better than the 0.8° in the raw dataset). The application of quaternion averaging and the Kuwahara filter to PED, an orientation microscopy technique with superior spatial resolution, is highly novel. In order to understand the influence of the Kuwahara filter on the results, various artificial datasets (i.e. single crystals, bicrystals and gradient crystals) with a random distribution of misorientations less than the noise level have been simulated. The probability (P) of all misorientation variations ($\Delta\theta$) is equal (i.e. for example $P_{\Delta\theta=0.1^\circ} = P_{\Delta\theta=0.8^\circ}$). While the results of these simulations are extensive and will be reported elsewhere, the key conclusions are: (i) the size of the sub-region selected for the Kuwahara filter should match the size of the cells/grains; (ii) it is essential to avoid "over-filtering", which can be assessed by tracking the improvement in the angular resolution while preserving real orientations that exist between cells; and (iii) the minimum real disorientation that can be distinguished from noise (<0.8°) using the Kuwahara filter is 0.4°. This last point is important when understanding the dislocation densities that can be measured using this technique. This uncertainty (0.4° here) can be correlated with a dislocation density of $\sim 10^{15}$ m^{-2}, and thus can be propagated through and displayed as a reliability map, where the higher numbers represent calculations with greater reliability or certainty (see Fig. 4).

4.3. Dislocation density maps and correlations

4.3.1. Dislocation density maps

An index map of commercially pure UFG Ti is shown in Fig. 5a, and contains grains whose size ranges from ~100 nm to ~2 μm. The calculated dislocation density distribution map has been overlaid with the TSL reconstructed grain boundaries and is shown in Fig. 5b. The large elongated grain identified in Fig. 5a as region #1 is

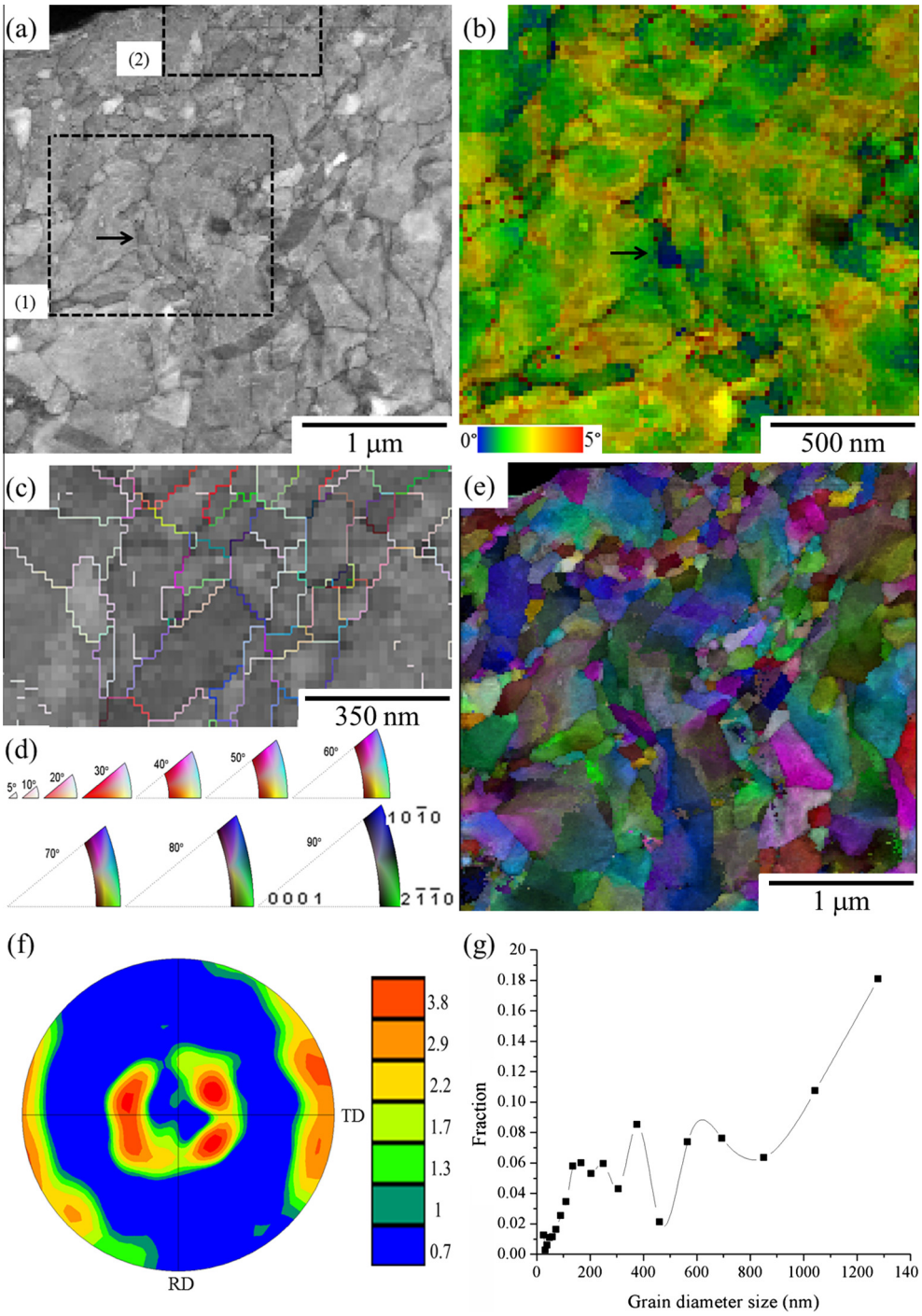

Fig. 3. PED results with a scanning step size of 10 nm of a severely deformed commercially pure α-Ti alloy, including (a) index map, (b) kernel average misorientation plot of the sub-region labeled 1 in "a", (c) grain boundary representation in quaternion color of the sub-region labeled 2 in "a", and (d) color legend, which depicts homophase misorientations made by stereographic projections of sections of constant disorientation angle used to interpret the "c" and "e" plots. Based on the color legend, the variation in the misorientation angle and the misorientation axis can be interpreted. (e) Quaternion misorientation plot of "a"; (f) texture plot shows the deviation of $\{11\bar{2}1\}$ pole from normal direction; and (g) the grain diameter size distribution. (For interpretation of the references to color in this figure legend, the reader is referred to the web version of this article.).

shown in detail in Fig. 5c and contains a uniform distribution of dislocation cells. A second region identified as #2 and shown in Fig. 5d is markedly different. Region #2 contains many black pixels, indicating a lack of dislocations due to the fact that the calculated dislocation densities are less than the minimum dislocation density resolvable.

Another example of the ability of the dislocation density distribution code to differentiate spatially varying disorientations, and thus dislocation densities, is shown in Fig. 6a,b. A small part of a PED orientation database was segmented and is shown in the quaternion misorientation plot in Fig. 6a. The resultant dislocation density

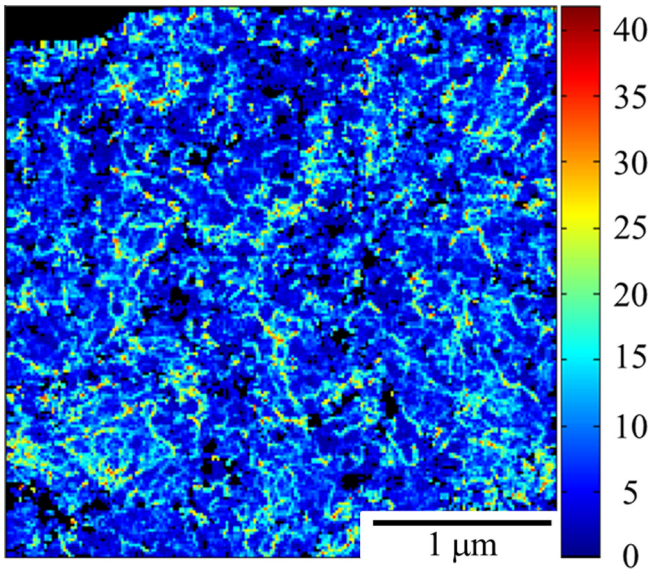

Fig. 4. Reliability map of the dislocation density distribution of the dataset shown in Fig. 3a. The scale bar values represent the ratio between the calculated dislocation density and the approximate lower dislocation density resolution (10^{15} m^{-2}).

distribution plot is given in Fig. 6b. The point-to-point and point-to-origin measurements along two vectors labeled #1 and #2 in Fig. 6a, which are located inside regions $\boldsymbol{R_1}$ and $\boldsymbol{R_2}$, exhibit maximum disorientations of 4° and ~0.1°, respectively. The dislocation density plot shown in Fig. 6b shows a region with a high dislocation density ($\boldsymbol{R_1}$) and a region with a low dislocation density ($\boldsymbol{R_2}$). These examples point to the potential of this method to determine microstructure–defect structure correlations, helping to identify the origin of spatially varying dislocation populations. For example, for these two observations, a reasonable inquiry is whether the population differences arise from the size of the grains (thus, an "average" descriptor-mediated correlation) or are due to the orientations and "strength" of the neighboring grains (thus, a correlation requiring higher-order descriptors [50,51]). PED-derived dislocation density data is extendible to a wide variety of structural alloys, including Ni-based superalloys, Ti-based alloys, Al-based alloys, Mg-based alloys and for many different problems (e.g. UFG materials, creep, fatigue and dwell fatigue) [7,8,10,52–73].

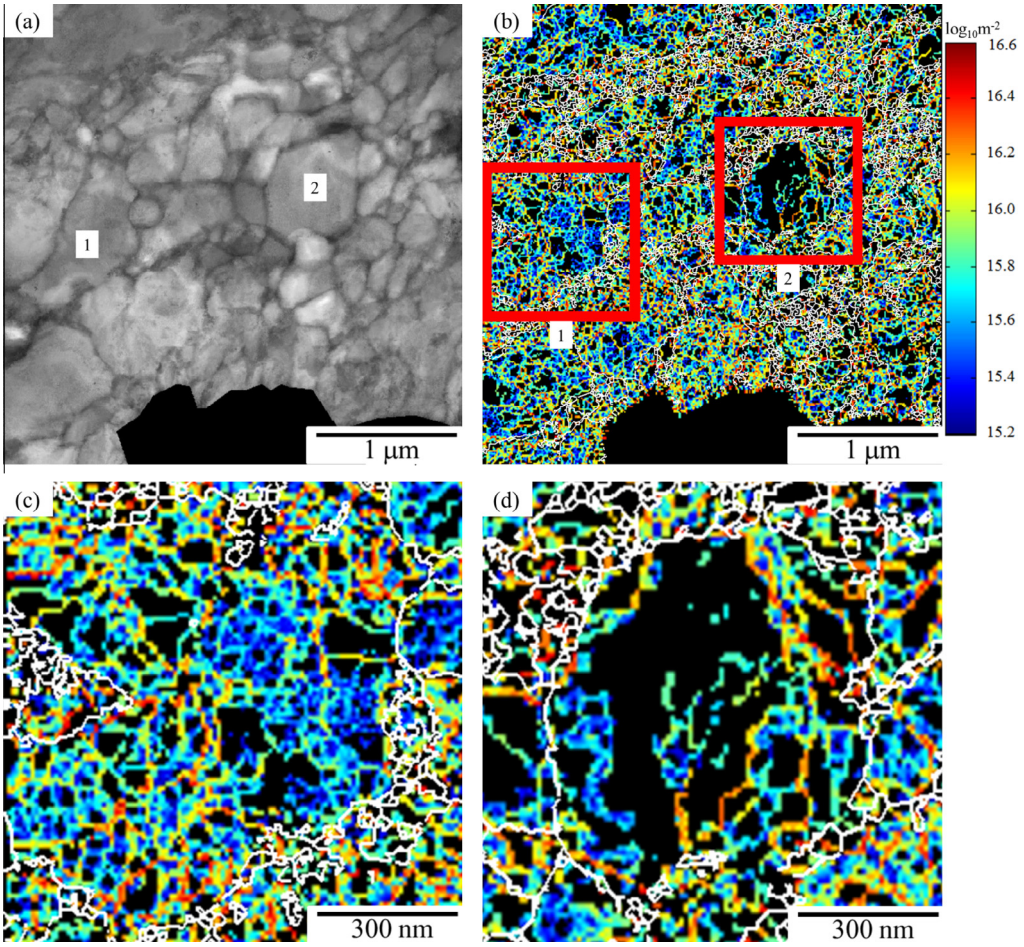

Fig. 5. An example of the procedure described in this paper applied to the acquired PED scan of a UFG Ti material. (a) The index map shows the variation in grain size. The PED scan step size is 10 nm. (b) The dislocation density distribution map overlaid with reconstructed grain boundaries. Similar size grains indicated in (a) by 1 and 2 have completely different dislocation networks in (b). (c) Magnified view of region 1, and (d) magnified view of region 2. Note that black pixels in (b)–(d) indicate data that falls below the estimated detection limit, and that white pixels indicate grain boundaries.

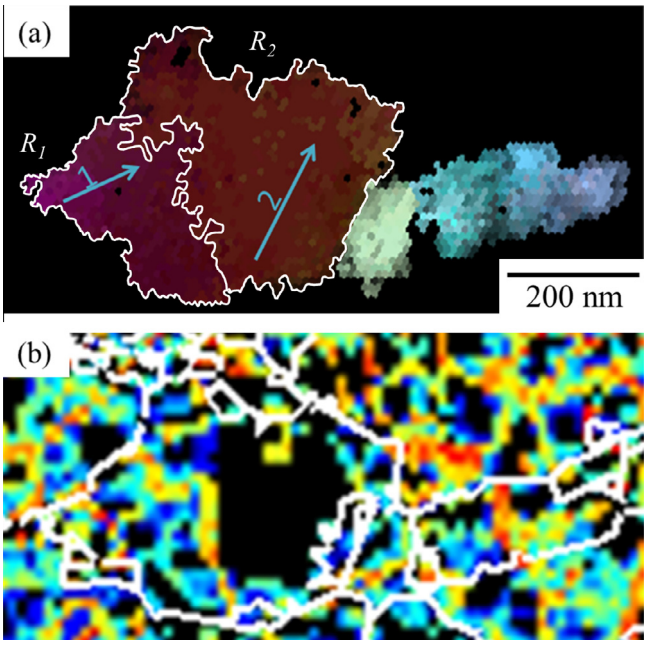

Fig. 6. Verification of the proposed method to calculate dislocation density distribution (a) quaternion misorientation of a segmented region of an orientation database. The maximum point-to-point and point-to-origin misorientation along lines 1 and 2 are 4° and ~0.1°, respectively. (b) The left grain mentioned in (a) has a region that is full of dislocations and a region that is depleted of dislocations. This example clearly shows the consistencies between the expected and calculated dislocation densities. Note that black pixels (b) indicate data that falls below the estimated detection limit, and that white pixels indicate grain boundaries.

Other microstructure–defect structure correlations can be deduced easily. For example, the dislocation density distribution map of the same region shown in Fig. 3b is represented in Fig. 7. In such a map, it is possible to determine regions containing few GNDs (sub-region labeled "1"), cellular structure and cell walls/sub-grain boundaries (sub-region labeled "2"), and hot and cold spots (sub-region labeled "3").

4.3.2. Other representation schemes for the data

One quantitative metric of GND density distribution is the distribution of dislocation densities vs. the smallest Euclidean distance to grain boundaries and triple junctions [19]. The distances of each pixel from the closest reconstructed grain boundary and triple junction were calculated using a watershed transform method (Fig. 8a,b). The statistical distribution of dislocations with respect to the reconstructed grain boundaries and triple junctions are shown in Fig. 8c,d, where the color indicates counts. The minimum Euclidean distance calculated is slightly greater than the step size of the PED scan (i.e. poorer resolution), due to the requisite conversions between grid types and the inconsistencies that arise as a result of the maximum boundary deviation parameter needed to digitally reconstruct the grain boundaries. As expected, the dislocations mostly accumulate close to grain boundaries and triple junctions (see Fig. 8c,d).

In addition to extracting distance maps of the data, in theory it is possible to deduce the dominant types of dislocations present in the material, as shown graphically in Fig. 9. In the experiments, although the beam is precessing, its angle from the optical axis is quite small. Effectively, one can consider an average beam orientation that is being used to probe the material, and from which it is possible to

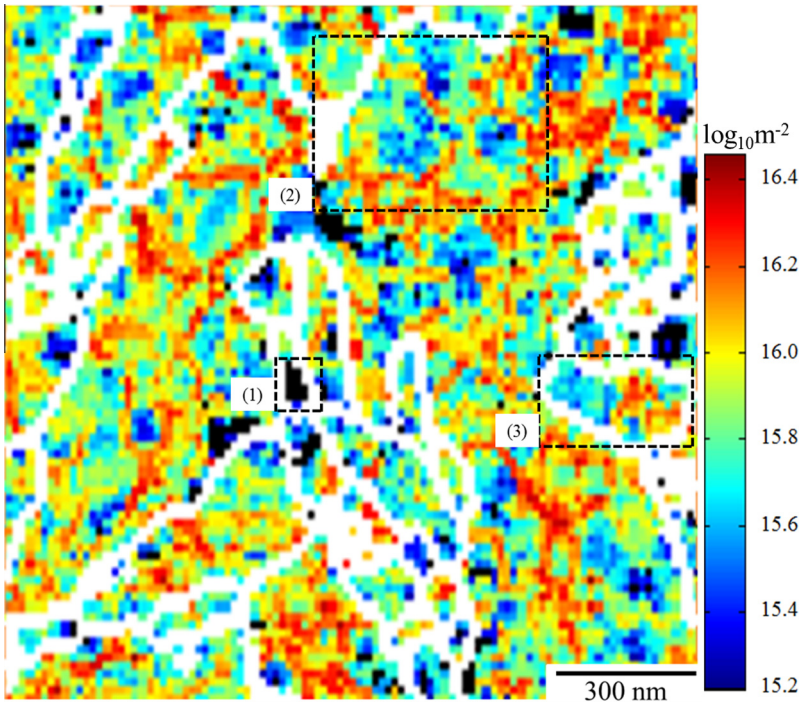

Fig. 7. Dislocation density distribution map represents dislocation architecture network. A region containing few geometrically necessary dislocations (sub-region 1), a cellular structure and cell walls/sub-grain boundaries (sub-region 2) and the location of hot and cold spots (sub-region 3) are shown. Note that black pixels indicate data that falls below the estimated detection limit, and that white pixels indicate grain boundaries.

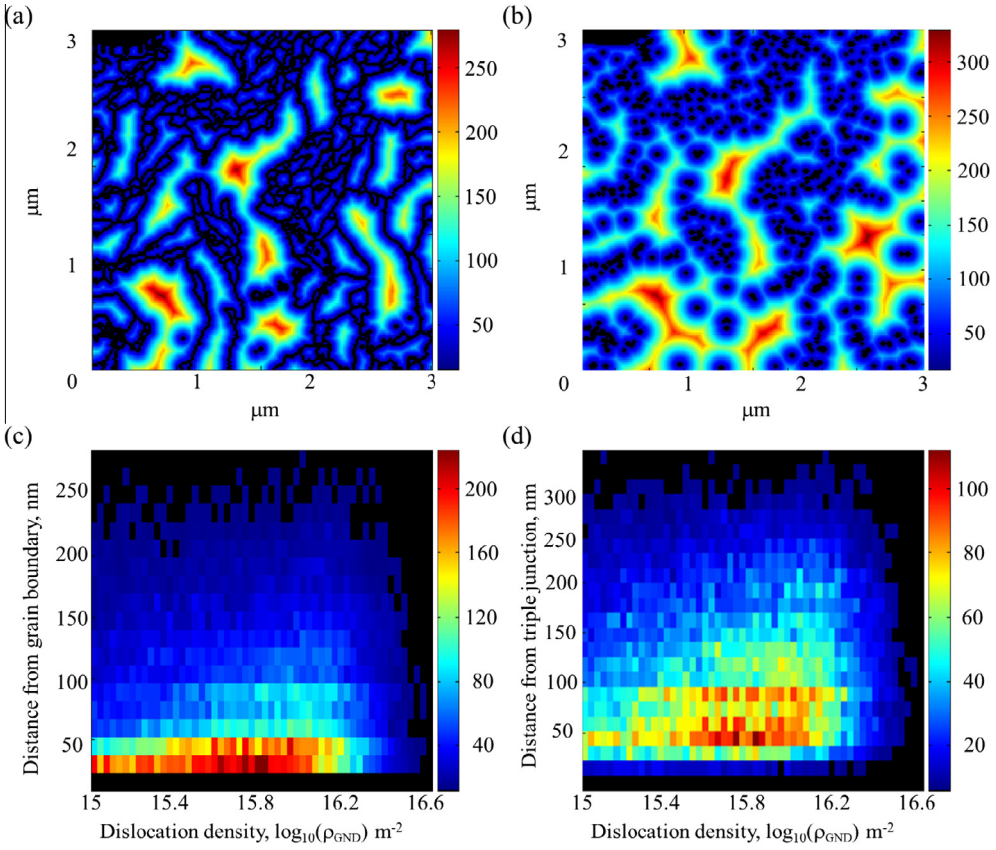

Fig. 8. Quantitative representation of dislocation density distribution with respect to grain boundaries and triple junctions conducted on the dataset used for Fig. 3. (a) Watershed transform method is applied to calculate the closest distance of pixels from the reconstructed grain boundaries. (b) Similar procedure as in (a) for triple junctions. (c) Distance from the closest reconstructed grain boundary vs. dislocation density. The bin width in x and y axes are 0.03 in $\log_{10}$ scale and 15 nm, respectively. (d) Similar to (c) for triple junctions.

extract lattice curvatures and therefore deduce GND densities, as has been demonstrated above. If we consider slip occurring on a given plane (i.e. $\langle \boldsymbol{a} \rangle$-type dislocations gliding on the basal plane in hcp Ti), the largest amount of lattice curvature (and hence GND densities) will be observed when looking along the basal plane (not the basal plane normal). Fig. 9 shows the deviation of the viewing directions that lead to the given dislocation densities plotted along the c-axis (i.e. 0001) projection. The observations made at the perimeter of this plot show the predominance of $\langle \boldsymbol{a} \rangle$-type slip on the 0001 plane, although some clusters toward the interior part of this representation can be identified as likely to be $\langle \boldsymbol{a} \rangle$-type dislocations on $10\bar{1}1$ planes, $\langle \boldsymbol{c}+\boldsymbol{a} \rangle$-type on $11\bar{2}2$ planes, and twinning on $10\bar{1}2$ planes. The spread of $\langle \boldsymbol{a} \rangle$-type dislocations away from the perimeter of the pole figure suggests a complex dislocation structure (sub-grain boundaries) comprised almost entirely of $\langle \boldsymbol{a} \rangle$-type dislocations, leading to lower energy.

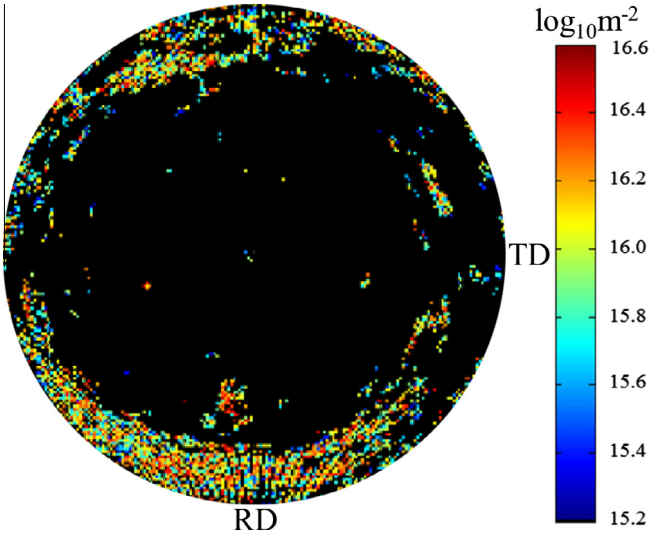

Fig. 9. A plot of the rotation basal planes (represented by their normal) from the beam direction. The measurable dislocation densities on the perimeter of this representation indicate a predominance of $\langle \boldsymbol{a} \rangle$-type dislocations on the basal plane. The clusters toward the interior part of this representation can likely be identified as $\boldsymbol{a}$-type dislocations on $10\bar{1}1$, $\langle \boldsymbol{c}+\boldsymbol{a} \rangle$-type on $11\bar{2}2$ and twinning on $10\bar{1}2$ planes.

5. Challenges and limitations

The application of PED-acquired datasets to extract dislocation densities of severely deformed materials and their correlations with microstructural features have not been shown previously in the literature. For completeness, two potential challenges and limitations require discussion, namely an assessment of dislocation density resolution

and whether "bend contours" (a TEM artifact) will influence the datasets for these materials.

5.1. Dislocation density resolution

Since GND density is proportional to local lattice curvature, it can be argued (accurately, if limiting the argument to bulk dislocation density, and erroneously, if applied to spatially resolved dislocation content) that scanning step size significantly affects the calculated GND density [16]. Indeed, step size plays a key role in GND density calculations according to Nye's formulation. Large step sizes increase the risk of losing information related to the dislocation network as it may miss dislocation dipoles separated by a small dimension [38]. However, dislocation density calculations for datasets collected using small step sizes may be susceptible to noise, artificially increasing the calculated dislocation density. The minimum resolvable GND density that has been reported previously as a function of angular resolution and step size is presented in the following equation [38,74]:

$$\rho_{\min}^{GND} = \frac{\text{Angular resolution (rad)}}{\text{Step size} * \text{Burger's vector length}}. \quad (10)$$

Based on this equation, the dislocation density resolution of a PED scan with step size of 10 nm before and after applying quaternion averaging is $\sim 4.7 \times 10^{15}$ and $\sim 2.3 \times 10^{15}\ \mathrm{m}^{-2}$, respectively, as the angular resolution improves from 0.8° to 0.4°. Obviously, improving the angular resolution is critical to accurately quantifying and mapping dislocation density. Eq. (10) leads to a conclusion that the step size must be selected depending upon the expected dislocation density of the studied material [38]. For example, He et al. [74] have criticized the use of a step size of 20 nm instead of 1 μm to study dislocation density of a 5% cold-rolled aluminum due to increasing the lower bound of dislocation density from 6.1×10^{13} to $3 \times 10^{15}\ \mathrm{m}^{-2}$, respectively. This level of spatial resolution is appropriate to study dislocation density of slightly deformed materials. However, for severely deformed materials (or localized regions with a high degree of deformation) in which the local orientation gradient is measurable, far smaller step sizes are more appropriate. As the spatial resolution has increased significantly, the argument of Eq. (10) must be applied to a "window" for which lattice curvatures are being measured, as opposed to the bulk specimen. Thus, for a dislocation content of two or more dislocations within the thickness of the specimen, the local dislocation density surpasses the threshold deduced by Eq. (10), and thus the approach is valid.

In the case of highly deformed UFG materials where high dislocation densities are expected, smaller step sizes (e.g. 2–15 nm) are not only preferable, but also provide critical details of the deformation structure. Any noise present does not mask important dislocation density information as the dislocation densities calculated for regions in which the dislocation density is low or negligible (e.g. recrystallized grains) are eliminated as they fall below the dislocation density resolution. In practice, if the resolution improves to 0.2°, the missing points are related to a single dislocation line segment for a given probed volume. Consequently, this current approach does not capture mobile SSDs with the current resolution. However, there is the potential to capture them if the angular resolution improves for the raw data—a significant advantage over EBSD-based techniques which invariably miss SSDs: as SSDs exist in dipoles and multiples with no net Burgers vector, they cannot be detected if the step size is not small enough to separate these dipoles from each other [38,75].

5.2. Bend contours

In addition to the challenges regarding intrinsic resolution of the data, an additional challenge and limitation of the methods described in this paper is the presence of "bend contours" that are regularly found in ductile thin foil specimens, and thus should be considered as potentially contributing to dislocation density calculations. However, their presence in highly deformed UFG materials is not immediately obvious, and the likelihood of their presence in these materials will be discussed.

Briefly, bend contours are real-space observations of Kikuchi diffraction patterns in TEM specimens. As their name implies, they are small, localized, permanent bends that are present within the specimen. When present, bend contours indicate that lattice curvature and thus disorientations are present, which ultimately could result in the calculation of dislocation densities that are an artifact of specimen preparation, contributing to the overall dislocation density. The magnitude of the strains that are present at the surface of the bend contours can be approximated using the following approach.

In bending, the maximum stress is located at the surfaces of the object, and is under compression on one surface and under tension on the other surface. The stress varies linearly between these maximum opposing stresses and passes through a value of 0 at the "neutral surface" located within the body of the object. The radius of curvature ρ is related to the curvature κ, the infinitesimal change in the angle between the surface normal $d\theta$ and the infinitesimal distance along the curve (which can be approximated as the infinitesimal distance along a length dx) as shown in the following equation:

$$\kappa = \frac{1}{\rho} = \frac{d\theta}{ds} \approx \frac{d\theta}{dx}. \quad (11)$$

The curvature κ can then be related to the longitudinal strain according to:

$$\varepsilon_x = -\frac{y}{\rho} = -y.\kappa, \quad (12)$$

where ε_x is the 1-D strain along the curved surface and y is the distance from the neutral surface ($\lceil = 0$) from the object surface.

In electron diffraction, it is possible to directly calculate each of these parameters to estimate the magnitude of the strains present in the specimen. As the subject is one of bend contours, it is first necessary to consider the change in angle along the surface. As bend contours are directly related to the Kikuchi lines, which are due to Bragg diffraction in thicker specimens, the angle can be calculated readily according to Bragg's law:

$$n\lambda = 2d \sin\theta, \tag{13}$$

where λ is the wavelength ($\lambda = 0.00251$ nm for 200 kV), d is the d-spacing and θ is the diffraction angle. Although d-spacings can vary considerably, for the purposes of this exercise, a reasonable value to take for the d-spacing would be 0.15 nm, which will give a diffraction angle of 0.0085 radians. It is common for bend contours to exhibit a real-space distance between a $+\mathbf{g}$ and $-\mathbf{g}$ diffraction event 2θ of ~500–1000 nm. Thus, a reasonable value to take as the distance between the true normal and $+\theta$ is half the bend contour thickness (i.e. $x = 300$ nm). This gives a curvature κ of $\sim 2.84 \times 10^{-5}$ rad nm^{-1}. For a 150 nm thick specimen ($y \approx 75$ nm), the strain ε_x is then $\sim 2 \times 10^{-3}$. This value goes down as the specimens get thinner, the d-spacing increases or the bend contour thickness decreases. Other reasonable values ($d = 2.25$ Å, $x = 500$ nm, $y = 50$ nm) produce strains that are a fraction of this value $\varepsilon_x \approx 5 \times 10^{-4}$. Clearly, the strains are very small.

While the values suggest strains in the elastic regime, the bend contours are permanent, indicating that plastic deformation has occurred, even if the stress imposed on the material is less than the yield strength ($\sigma_{ys}^{0.2\%}$). While it is exceptionally difficult to prove, a reasonable assumption is that the probability of producing bend contours decreases as the resistance to deformation as indicated by the yield strength ($\sigma_{ys}^{0.2\%}$) increases. Thus, for highly deformed high-strength materials, bend contours are unlikely.

6. Conclusions

These results demonstrate, for the first time, the extensibility of a novel TEM-based orientation imaging technique, PED, to characterize UFG metallic materials (specifically titanium) and extract spatial variations of dislocation densities. Following a series of post-processing steps, it is possible to extract maps of dislocation density with an ultimate spatial resolution of ~1–2 nm. Such capability has not been presented previously in the literature. The extraction of such maps can be subsequently interrogated to understand deformation structure–microstructure correlations. This has been demonstrated by plotting dislocation density vs. the distance away from grain boundaries and triple junctions. The data seems to scale with previous observations from high-resolution EBSD data plotted in a similar way. By plotting dislocation density as a function of local crystal orientation, it is possible to present dislocation density as a pole figure and deduce contributions of different deformation mechanisms. In addition, it is clearly possible to visualize new, nascent grains in highly deformed materials, as well as make new observations of grains where one region has no dislocation activity and another part has a substructure. Such observations point to the need to understand defect structure correlation with microstructure using higher-order correlation functions (e.g. to understand the effect of nearest-neighbor grains on the deformation of any arbitrary grain).

Acknowledgments

The authors gratefully acknowledge the University of North Texas; the Air Force Research Laboratory; the Center for Advanced Non-Ferrous Structural Alloys, which is a joint industry-university center between the Colorado School of Mines and the University of North Texas (NSF award no. 1134873); and the Center for Advanced Research and Testing at the University of North Texas. In addition, the authors gratefully acknowledge invaluable discussions with Prof. Anthony Rollett on the topic of symmetry. The authors also acknowledge the thoughtful and helpful review given during the peer-review process for the publication of this manuscript.

References

[1] Hirsch P, Cockayne D, Spence J, Whelan M. Philos Mag 2006;86:4519.
[2] Tanner LE. Philos Mag 1966;14:111.
[3] Wilkinson AJ, Hirsch PB. Micron 1997;28:279.
[4] Britton TB, Birosca S, Preuss M, Wilkinson AJ. Scripta Mater 2010;62:639.
[5] Yoshimura H, Nakahigashi J. Int J Hydrogen Energy 2002;27:769.
[6] Valiev RZ, Estrin Y, Horita Z, Langdon TG, Zechetbauer MJ, Zhu YT. JOM 2006;58:33.
[7] Stolyarov VV, Zhu YT, Alexandrov IV, Lowe TC, Valiev RZ. Mater Sci Eng, A 2003;343:43.
[8] Sabirov I, Perez-Prado M, Molina-Aldareguia J, Semenova I, Salimgareeva GK, Valiev R. Scripta Mater 2011;64:69.
[9] Chen Y, Li Y, Walmsley J, Dumoulin S, Skaret P, Roven H. Mater Sci Eng, A 2010;527:789.
[10] Sergueeva A, Stolyarov V, Valiev R, Mukherjee A. Scripta Mater 2001;45:747.
[11] Kim I, Kim J, Shin D, Liao X, Zhu Y. Scripta Mater 2003;48:813.
[12] Purcek G, Saray O, Kul O, Karaman I, Yapici G, Haouaoui M, et al. Mater Sci Eng, A 2009;517:97.
[13] Terada D, Inoue S, Tsuji N. J Mater Sci 2007;42:1673.
[14] Ko YG, Shin DH, Park K-T, Lee CS. Scripta Mater 2006;54:1785.
[15] Taylor GI. Proc R Soc A 1934;145:362.
[16] Guruprasad P, Benzerga A. J Mech Phys Solids 2008;56:132.
[17] Gubicza J, Dragomir I, Ribárik G, Baik S, Zhu Y, Valiev R, et al. Z Metallkd 2003;94:1185.
[18] Ungár T, Gubicza J, Ribárik G, Borbély A. J Appl Crystallogr 2001;34:298.
[19] Jiang J, Britton T, Wilkinson A. Acta Mater 2013;61:7227.
[20] Humphreys F, Huang Y, Brough I, Harris C. J Microsc 1999;195:212.
[21] Zaefferer S. Ultramicroscopy 2007;107:254.

[22] Liu X, Nuhfer N, Rollett A, Sinha S, Lee S-B, Carpenter J, et al. Acta Mater 2013;64:333.
[23] Wright SI. J Comput-Assisted Microscopy (USA) 1993;5:207.
[24] Hurley P, Humphreys F. Acta Mater 2003;51:1087.
[25] Wilkinson AJ, Britton TB. Mater Today 2012;15:366.
[26] Littlewood P, Britton T, Wilkinson A. Acta Mater 2011;59:6489.
[27] Littlewood P, Wilkinson A. Acta Mater 2012;60:5516.
[28] Britton T, Liang H, Dunne F, Wilkinson A. Proc R Soc A: Math Phys Eng Sci 2010;466:695.
[29] Katrakova D, Mucklich F, Damgaard M. Sonderb Prakt Metallogr 2001:355.
[30] Viladot D, Véron M, Gemmi M, Peiró F, Portillo J, Estradé S, et al. J Microsc 2013;252:23.
[31] Rauch EF, Portillo J, Nicolopoulos S, Bultreys D, Rouvimov S, Moeck P. Z Kristallogr 2010;225:103.
[32] Meredith CS, Khan AS. Int J Plast 2012;30:202.
[33] Williams DB, Carter CB. Transmission electron microscopy. 2nd ed. Berlin: Springer Verlag; 2009.
[34] Humphreys F, Bate P, Hurley P. J Microsc 2001;201:50.
[35] Brough I, Bate P, Humphreys F. Mater Sci Technol 2006;22:1279.
[36] Pharr GM, Herbert EG, Gao Y. Annu Rev Mater Res 2010;40:271.
[37] Gao H, Huang Y. Scripta Mater 2003;48:113.
[38] Adams BL, Kacher J. Comput Mater Con 2010;14:185.
[39] Ashby M. Philos Mag 1970;21:399.
[40] Pantleon W. Scripta Mater 2008;58:994.
[41] Calcagnotto M, Ponge D, Demir E, Raabe D. Mater Sci Eng, A 2010;527:2738.
[42] Jorge-Badiola D, Iza-Mendia A, Gutiérrez I. Mater Sci Eng, A 2005;394:445.
[43] Benjamin Britton T, Wilkinson AJ. Acta Mater 2012;60:5773.
[44] Pougis A, Toth L, Fundenberger J, Borbely A. Scripta Mater 2014;72:59.
[45] Glavicic M, Kobryn P, Bieler T, Semiatin S. Mater Sci Eng, A 2003;346:50.
[46] Wright SI, Nowell MM, Field DP. Microsc Microanal 2011;17:316.
[47] Patala S, Schuh CA. Acta Mater 2011;59:554.
[48] Rohrer GS, Saylor DM, El-Dasher B, Adams BL, Rollett AD, Wynblatt P. Z Metallkd 2004;95:197.
[49] Beladi H, Rohrer GS, Rollett AD, Tari V, Hodgson PD. Acta Mater 2014;63:86.
[50] Niezgoda SR, Kanjarla AK, Kalidindi SR. Integ. Mater. Manuf. Innovation 2013;2:1.
[51] Panchal JH, Kalidindi SR, McDowell DL. Comput Aided Des 2013;45:4.
[52] Unocic R, Kovarik L, Shen C, Sarosi P, Wang Y, Li J, et al. Superalloys 2008;8:377.
[53] Viswanathan G, Sarosi P, Henry M, Whitis D, Milligan W, Mills M. Acta Mater 2005;53:3041.
[54] Ma Z, Pilchak A, Juhas M, Williams J. Scripta Mater 2008;58:361.
[55] Jiang H, Garcia-Pastor F, Hu D, Wu X, Loretto M, Preuss M, et al. Acta Mater 2009;57:1357.
[56] Yuan W, Mishra RS, Carlson B, Mishra R, Verma R, Kubic R. Scripta Mater 2011;64:580.
[57] Charit I, Mishra RS. Acta Mater 2005;53:4211.
[58] Furukawa M, Iwahashi Y, Horita Z, Nemoto M, Tsenev NK, Valiev RZ, et al. Acta Mater 1997;45:4751.
[59] Gholinia A, Humphreys F, Prangnell P. Acta Mater 2002;50:4461.
[60] Lee S, Utsunomiya A, Akamatsu H, Neishi K, Furukawa M, Horita Z, et al. Acta Mater 2002;50:553.
[61] Venkatramani G, Ghosh S, Mills M. Acta Mater 2007;55:3971.
[62] Dunne F, Rugg D. Fatigue Fract Eng Mater Struct 2008;31:949.
[63] Venkataramani G, Kirane K, Ghosh S. Int J Plast 2008;24:428.
[64] Anahid M, Samal MK, Ghosh S. J Mech Phys Solids 2011;59:2157.
[65] Čížek J, Prochazka I, Smola B, Stulíková I, Kužel R, Matěj Z, et al. Mater Sci Eng, A 2007;462:121.
[66] McBagonluri F, Akpan E, Mercer C, Shen W, Soboyejo W. Mater Sci Eng, A 2005;405:111.
[67] Unocic R, Viswanathan G, Sarosi P, Karthikeyan S, Li J, Mills M. Mater Sci Eng, A 2008;483:25.
[68] Valiev R, Korznikov A, Mulyukov R. Mater Sci Eng, A 1993;168:141.
[69] Deka D, Joseph DS, Ghosh S, Mills MJ. Metall Mater Trans A 2006;37:1371.
[70] Han B, Mohamed F, Lee Z, Nutt S, Lavernia E. Metall Mater Trans A 2003;34:603.
[71] Sinha V, Mills M, Williams JC, Spowart J. Metall Mater Trans A 2006;37:1507.
[72] Unocic KA, Hayes RW, Mills MJ, Daehn GS. Metall Mater Trans A 2010;41:409.
[73] Liu H, Mishnaevsky Jr L. Acta Mater 2014;71:220.
[74] He W, Ma W, Pantleon W. Mater Sci Eng, A 2008;494:21.
[75] Kacher J, Landon C, Adams BL, Fullwood D. Ultramicroscopy 2009;109:1148.